



Diagnostic Relations for the Intercept Parameter of Exponential Raindrop Size Distribution According to Rain Types Derived from Disdrometer Data and Their Impacts on Precipitation Prediction

Joohyun Lee¹ · Han-Gyul Jin¹ · Jong-Jin Baik¹

Received: 13 June 2022 / Revised: 4 October 2022 / Accepted: 20 November 2022 / Published online: 5 December 2022
© The Author(s) 2022

Abstract

The raindrop size distribution observed from ground-based or airborne disdrometers has been widely used to understand the characteristics of clouds and precipitation. However, its variability needs to be studied further and properly considered for improving precipitation prediction. In this study, using disdrometer data, the diagnostic relations for the intercept parameter of the exponential raindrop size distribution N_0 are derived for different rain types and the impacts of the diagnostic relations on precipitation prediction are examined. The disdrometer data observed at four sites in South Korea show spatiotemporal variations of N_0 . Three different derivation methods proposed by previous studies are used to derive the diagnostic relations, and the diagnostic relation that best reproduces the observed N_0 is selected. The diagnostic relation is implemented into the WRF single-moment 6-class microphysics (WSM6) scheme, and its impacts are investigated through the simulations of summertime precipitation events in South Korea. Compared to the simulation using the original WSM6 scheme (WSM6-O) where a constant N_0 is used, the simulation where N_0 is diagnosed by the diagnostic relation using the rainwater content at the lowest level (WSM6-L) yields better precipitation prediction. The WSM6-L simulation represents the variability of N_0 . Also, the WSM6-L simulation predicts N_0 that is on average smaller than the prescribed value in the WSM6-O simulation, agreeing with the observation to some extent. The smaller N_0 in the WSM6-L simulation decreases the rainwater production by the accretion of cloud water and the melting of ice hydrometeors, decreasing the rainwater mixing ratio.

Keywords Raindrop size distribution · Intercept parameter · Disdrometer · Bulk cloud microphysics · Precipitation prediction

1 Introduction

There are two main methods of explicitly representing cloud microphysical processes in numerical models: the bin microphysics method and the bulk microphysics method. In models with bin microphysics schemes, hydrometeor of any type is subdivided according to its size and the number concentration of the hydrometeor in each size bin is prognostically calculated, thus the hydrometeor size distribution evolves naturally without any constraint. However,

because the bin microphysics method requires a vast amount of computational resources (Khain et al. 2015; Lee and Baik 2018; Grabowski et al. 2019), the bulk microphysics method, which is more economical, is commonly employed in weather and climate models. In models with bulk microphysics schemes, hydrometeor of any type is assumed to have a specific particle size distribution such as the exponential, gamma, or lognormal distribution. For example, the exponential size distribution of raindrops is given as

$$N(D) = N_0 \exp(-\Lambda D), \quad (1)$$

where N_0 is the intercept parameter and Λ is the slope parameter of raindrop size distribution (RSD). A well-known exponential distribution is the Marshall-Palmer distribution (Marshall and Palmer 1948), where N_0 is a fixed value of $8000 \text{ m}^{-3} \text{ mm}^{-1}$ and Λ is a function of rain rate.

Responsible Editor: Dong-Hyun Cha

✉ Jong-Jin Baik
jjbaik@snu.ac.kr

¹ School of Earth and Environmental Sciences, Seoul National University, 08826 Seoul, South Korea

In models with single-moment bulk microphysics schemes, which prognose only hydrometeor mixing ratios, the intercept parameter is usually fixed as in the Marshall-Palmer distribution and the slope parameter is determined by the prognosed rainwater mixing ratio.

The constant- N_0 assumption in single-moment bulk microphysics schemes is different from reality. Many studies have revealed that N_0 or the generalized intercept parameter N_w , which is computed from the rainwater content W and mass-weighted mean raindrop diameter D_m for a size distribution of any form and is identical to N_0 for an exponential size distribution, has a large spatiotemporal variability (Waldvogel 1974; Uijlenhoet et al. 2003; Loh et al. 2019; Chen et al. 2020; Suh et al. 2021; Jwa et al. 2021). Waldvogel (1974) observed a sudden change in N_0 , called the N_0 jump, during orographic precipitation when a convective portion within a precipitation system moved in to or out from a disdrometer site in Locarno, Switzerland. Uijlenhoet et al. (2003) also observed the N_0 jump at a disdrometer site in northern Mississippi, USA, when the transition from stratiform to convective rainfall occurred with the disappearance of the radar bright band. Chen et al. (2020) showed that N_0 and N_w decreased with altitude when landfalling typhoons passed the 356-m high meteorological tower in Shenzhen, China, where disdrometers are mounted at four different altitudes.

The analysis of data from a disdrometer in Seoul, South Korea, shows that N_0 fluctuates with rain rate and that the probability density function (PDF) of N_w have different characteristics depending on the rain type (i.e., stratiform, mixed, or convective) and weather type (Jwa et al. 2021). Suh et al. (2016) analyzed the data from a disdrometer in Busan and showed that the characteristics of N_w vary depending on the rain type and weather type and that N_w has clear seasonal and diurnal variability, which is attributed to changes in wind direction. Loh et al. (2019) compared the data from two disdrometers, one in the central region and the other in the southeastern region of the Korean Peninsula and showed that the mean value of N_w in the central region is larger than that in the southeastern region. Kim et al. (2022) investigated the microphysical characteristics of orographic rainfall over Mt. Halla where ten disdrometers are installed. They revealed that N_w at windward sites is overall smaller than that at leeward sites. Suh et al. (2021) analyzed data from four disdrometers installed in the southeastern region of the Korean Peninsula at an interval of ~20 km from the coastline to inland. They found that for stratiform rain, multiple peaks are seen in the N_w PDF in the coastal region while they are not seen in the inland area. They also found that for convective rain, the N_w value at which the peak appears decreases with the distance from the coastline.

The N_0 variability can be considered in a model by employing either a multi-moment microphysics scheme

or a diagnostic relation for N_0 . In models using multi-moment microphysics schemes, two or more moments of RSD are prognosed and N_0 is calculated from the prognosed moments, having a spatiotemporal variability. In models using single-moment microphysics schemes, a diagnostic relation for N_0 is required in order to represent the N_0 variability. There have been proposed several methods to derive a diagnostic relation for N_0 for use in single-moment microphysics schemes (Zhang et al. 2008; Abel and Boute 2012; Wainwright et al. 2014; Pan et al. 2016). Zhang et al. (2008, Z08 hereafter) proposed the moment relation method, in which it is assumed that two moments of RSD have a power-law relation. Using data from three disdrometers, they derived N_0 - W diagnostic relations from the power-law relation between RSD moments and showed that in comparison with the direct fitting of the N_0 - W relation, the moment relation method yields smaller biases in diagnosing N_0 . Abel and Boute (2012, AB12 hereafter) derived a power-law relation between N_0 and Λ using RSD data from aircraft, ground-based lidar, and disdrometer observations. Using the derived power-law relation between N_0 and Λ , N_0 is diagnosed from Λ in the Met Office Unified Model (Walters et al. 2019). In addition, there was an approach to obtain an optimal N_0 - Λ power-law relation by optimizing the coefficients in the relation using a micro-genetic algorithm and a harmony search algorithm (Jang et al. 2017). Pan et al. (2016) and Wainwright et al. (2014) established N_0 - W diagnostic relations using N_0 and W obtained from squall line and tornadic supercell simulations, respectively, that were run using a model with a double-moment microphysics scheme.

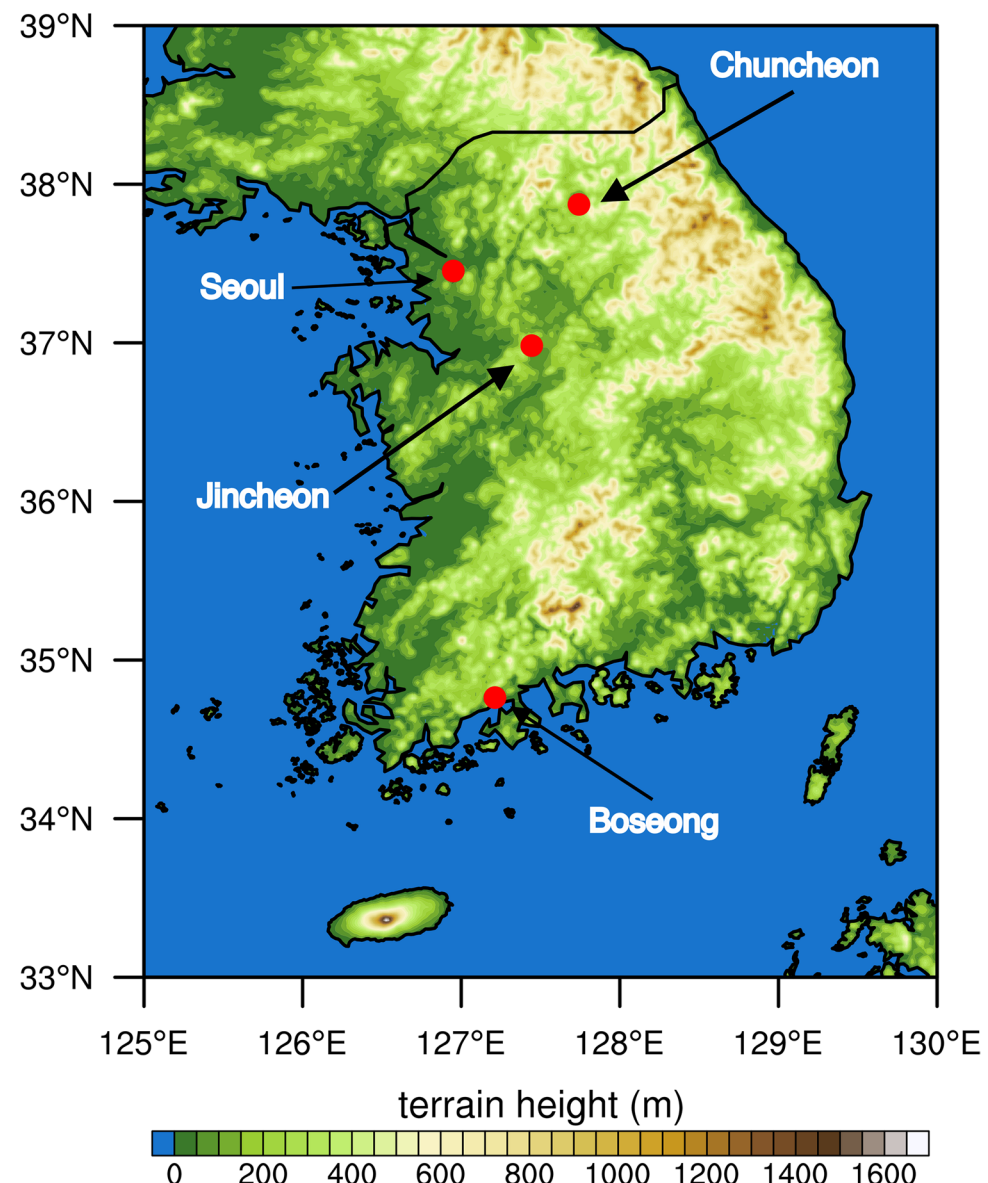
The implementation of a diagnostic relation for N_0 can improve the performance of a model with a single-moment microphysics scheme on precipitation prediction. In the numerical simulations of Abel and Boute (2012), the over-prediction of precipitation was reduced due to an increase of evaporation in the sub-cloud layer, which was attributed to the use of a diagnostic relation that represents large N_0 for light rain. Wainwright et al. (2014) evaluated a simulation where a diagnostic relation for N_0 was used by comparing it to a simulation with a double-moment microphysics scheme. Compared to the simulation using a fixed N_0 , the simulation using a diagnostic relation for N_0 yielded the predictions of cold pool size and strength that are more consistent with those in the simulation using a double-moment microphysics scheme.

Each of the aforementioned studies derived a single diagnostic relation for N_0 and applied to the simulations of various types of rain. Considering that the characteristics of N_w are different depending on the rain type (Bringi et al. 2003; Thurai et al. 2016; You et al. 2016; Jwa et al. 2021), the diagnosis of N_0 can be further improved if different diagnostic relations are derived for different rain types, which are done in this study. In addition, in this study, the several

derivation methods that were used in previous studies are tested to find out the diagnostic relation for N_0 that best represents the N_0 variability. The derived diagnostic relation for N_0 is used in the simulations of precipitation in South Korea, where the disdrometer sites at which the data used for the derivation were obtained are located, to examine the impacts of the diagnostic relation on regional precipitation prediction.

In Section 2, the disdrometer data and derivation methods used to obtain the diagnostic relations for N_0 are presented. In that section, the evaluation of the derived diagnostic relations is also given and the most appropriate diagnostic relation is chosen. In Section 3, the impacts of the diagnostic relations on precipitation prediction are investigated through the simulations of summer precipitation in South Korea. In Section 4, a summary and conclusions are given.

Fig. 1 Locations of four disdrometers (red circles) on the topographic map of South Korea and surrounding regions (shaded)



2 Diagnostic Relations for the Intercept Parameter N_0

2.1 Disdrometer Data

To derive diagnostic relations for N_0 , we collected disdrometer data from four sites in South Korea in 2019. The locations of the four sites are given in Fig. 1. The four disdrometers in Seoul, Chuncheon, Jincheon, and Boseong have been operated by the Convection and Urban Meteorology Group of Seoul National University, the Air Quality Prediction Research Laboratory of Kangwon National University, the Weather Radar Center of Korean Meteorological Administration, and the National Institute of Meteorological Sciences of Korean Meteorological

Administration, respectively. At all sites, the same type of disdrometer, Parsivel², is used. The Parsivel² disdrometer measures the diameter and fall speed of hydrometeors and classifies them into 32×32 bins of diameter and fall speed with non-uniform intervals (Tokay et al. 2014). The fall speed range is $0\text{--}22.4 \text{ m s}^{-1}$. The diameter range is $0.25\text{--}26 \text{ mm}$, and it is $0.25\text{--}8 \text{ mm}$ for liquid precipitation. The two smallest diameter bins ($0\text{--}0.25 \text{ mm}$) are excluded because of the low signal-to-noise ratio. The data sampling interval is 1 min. In this study, only liquid precipitation is considered. The quality control of the disdrometer data is conducted following Jwa et al. (2021). After the quality control, a total of 75,978 1-minute data remain and are used for the derivation of diagnostic relations for N_0 .

Figure 2 shows the box plots of N_0 estimated from the disdrometer data at the four sites for four seasons. The number of data for each site and season is also shown in this figure. Fall, summer, and spring account for large portions of the data, while winter does not. In the three seasons, the numbers of data at the four sites are similar to each other, except for Boseong in spring and Chuncheon in summer. The temporal and spatial variabilities of N_0 are revealed well in this figure. For the total data from all four sites, the median of N_0 for spring is $9,406 \text{ m}^{-3} \text{ mm}^{-1}$, which is larger than those for summer ($6,676 \text{ m}^{-3} \text{ mm}^{-1}$) and fall ($5,149 \text{ m}^{-3} \text{ mm}^{-1}$), which shows the seasonal variability of

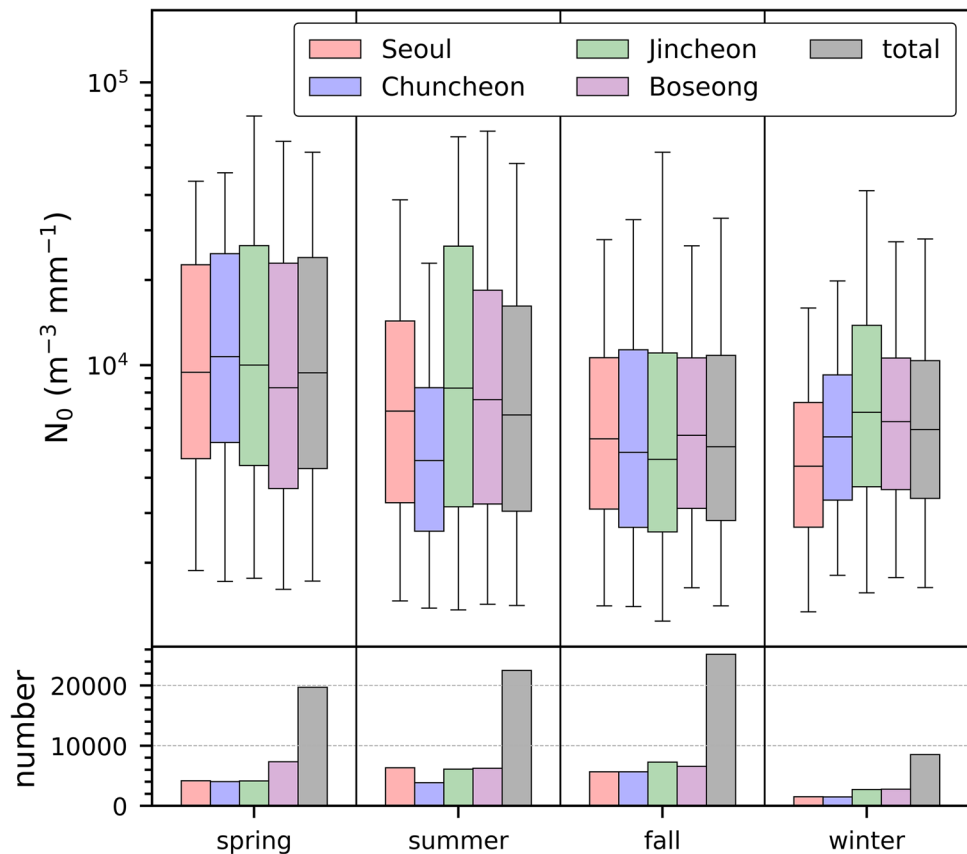
N_0 . The ranges between the 5th and 95th percentiles of N_0 for spring, summer, and fall are $1,724\text{--}56,741$, $1,413\text{--}51,695$, and $1,410\text{--}33,114 \text{ m}^{-3} \text{ mm}^{-1}$, respectively. This shows that N_0 significantly varies within the same season. The median of N_0 also differs depending on the site. In summer, for example, the medians of N_0 for Seoul, Chuncheon, Jincheon, and Boseong are $6,883$, $4,603$, $8,307$, and $7,553 \text{ m}^{-3} \text{ mm}^{-1}$, respectively. The large temporal and spatial variabilities of N_0 revealed in the disdrometer observations suggest that single-moment microphysics schemes in numerical models should not use the constant N_0 and allow N_0 to change with time and space.

2.2 Review of the Derivation Methods of Diagnostic Relations

To diagnose N_0 for single-moment microphysics schemes, N_0 should be expressed as a function of any variable such as the rainwater content W . In this study, we derive the $N_0\text{--}W$ diagnostic relations using three different methods proposed by previous studies (Zhang et al. 2008; Abel and Boutle 2012). For each method, we derive three diagnostic relations for different rain types, which was not done in the previous studies.

In the first method, the diagnostic relation between N_0 and W is determined by the direct fitting of the relation between

Fig. 2 Box plots of the intercept parameter N_0 estimated from the disdrometer data at the four sites and the total data for four seasons. The lower boundary, centerline, and upper boundary of boxes indicate the lower quartile, median, and upper quartile, respectively. The lower and upper whiskers represent the 5th and 95th percentiles, respectively. The number of each dataset is shown at the bottom



N_0 and W estimated from the disdrometer data (Zhang et al. 2008). The n th moment of RSD is expressed as follows:

$$M_n = \int D^n N(D) dD. \quad (2)$$

For the exponential RSD, Eq. (2) is expressed as

$$M_n = N_0 \Lambda^{-(n+1)} \Gamma(n+1), \quad (3)$$

where Γ is the gamma function. W is expressed as

$$W = \frac{\pi}{6} \rho_w M_3, \quad (4)$$

where ρ_w is the liquid water density. Following Zhang et al. (2008), the second and fourth moments of RSD are used to obtain Λ and N_0 as follows:

$$\Lambda = \left[\frac{M_2 \Gamma(5)}{M_4 \Gamma(3)} \right]^{\frac{1}{2}}, \quad (5)$$

$$N_0 = \frac{M_2 \Lambda^3}{\Gamma(3)}. \quad (6)$$

Based on N_0 and W estimated from the disdrometer data, the following power-law relation is obtained by a linear least-squares fitting for the logarithms of N_0 and W :

$$N_0 = \alpha_1 W^{\beta_1}. \quad (7)$$

Then, the coefficients α_1 and β_1 are determined.

In the second method, the diagnostic relation between N_0 and W is determined from the fitted N_0 - Λ relation (Abel and Boutle 2012). Based on N_0 and Λ estimated from the disdrometer data, the power-law relation of N_0 - Λ is obtained by a linear least-squares fitting for the logarithms of N_0 and Λ :

$$N_0 = a_2 \Lambda^{b_2}. \quad (8)$$

Substituting Eq. (3) for M_3 into Eq. (4) gives the relation between Λ and W :

$$\Lambda = \left(\frac{\pi \rho_w N_0}{W} \right)^{\frac{1}{4}}, \quad (9)$$

By substituting this relation into Eq. (8), the N_0 - W diagnostic relation from the fitted N_0 - Λ relation is obtained as follows:

$$N_0 = \alpha_2 W^{\beta_2}, \quad (10)$$

where

$$\alpha_2 = a_2^{\frac{4}{4-b_2}} (\pi \rho_w)^{\frac{-b_2}{b_2-4}}, \quad (11)$$

$$\beta_2 = \frac{b_2}{b_2 - 4}. \quad (12)$$

The third method to derive the diagnostic relation between N_0 and W is the moment relation method proposed by Zhang et al. (2008). Based on two different moments of RSD estimated from the disdrometer data, the power-law relation of the two moments is obtained by a linear least-squares fitting for the logarithms of the two moments:

$$M_l = a_3 M_m^{b_3}. \quad (13)$$

Substituting Eq. (3) into Eq. (13) and combining this equation with Eq. (9) gives the N_0 - W diagnostic relation as follows:

$$N_0 = \alpha_3 W^{\beta_3}, \quad (14)$$

where

$$\alpha_3 = \left[a_3 \frac{\Gamma^{b_3}(m+1)}{\Gamma(l+1)\pi^c \rho_w^c} \right]^{\frac{1}{1-b_3+c}}, \quad (15)$$

$$\beta_3 = \frac{c}{1-b_3+c}, \quad (16)$$

$$c = \frac{b_3(m+1)-(l+1)}{4}. \quad (17)$$

Note that $(l, m) = (2, 4)$ is used in this study. Hereafter, the diagnostic relation for N_0 derived by the direct fitting of the relation between N_0 and W is called DNW, and those derived using the N_0 - Λ relation and M_2 - M_4 relation are called DNL and DMM, respectively.

Many observational studies have shown that the characteristics of N_w differ depending on the rain type (Janapati et al. 2017; Seela et al. 2018; Lee et al. 2019; Jwa et al. 2021). To better represent the variability of the intercept parameter, the disdrometer data are divided into three rain types and then the aforementioned derivation methods are applied for each rain type. Tokay and Short (1996) showed that when the rain rate is lower (higher) than 1 (10) mm h⁻¹, stratiform (convective) rain is dominant and when the rain rate is between 1 and 10 mm h⁻¹, both rain types appear with similar frequency. Thus, we adopt the above criteria to classify the disdrometer data into stratiform, mixed, and convective rain, respectively, and a diagnostic relation for N_0 is derived for each rain type. The coefficients and exponents of the derived diagnostic relations for total, stratiform, mixed, and convective rain are given in Table 1.

2.3 Evaluation of the Derived Diagnostic Relations

Figure 3 shows the density scatter plots of N_0 and W estimated from the disdrometer data for the three rain types

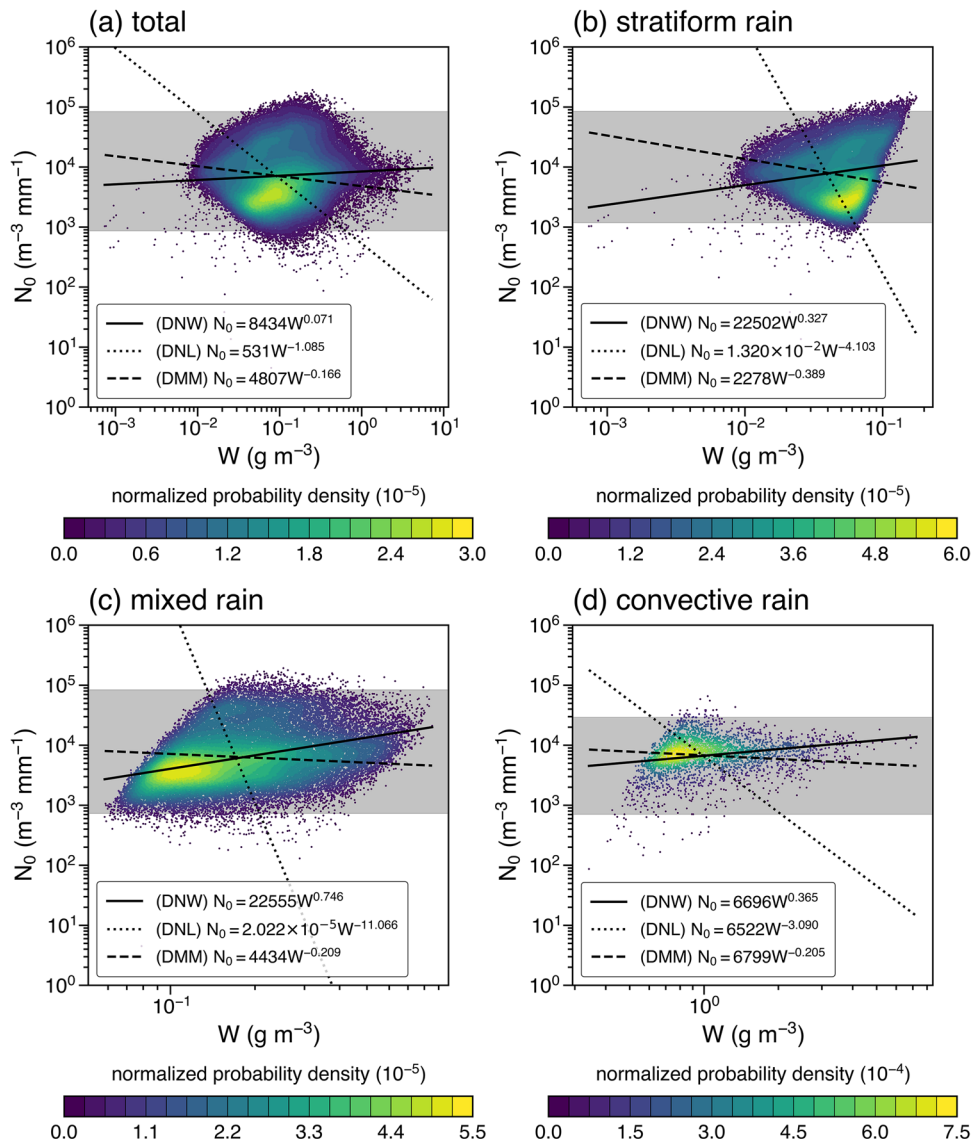
Table 1 Coefficients α_i and β_i in the derived diagnostic relations for total, stratiform, mixed, and convective rain

	DNW		DNL		DMM	
	α_1	β_1	α_2	β_2	α_3	β_3
total	8434	0.071	531	-1.085	4807	-0.166
stratiform	22502	0.327	1.320×10^{-2}	-4.103	2278	-0.389
mixed	22555	0.746	2.022×10^{-5}	-11.066	4434	-0.209
convective	6696	0.365	6522	-3.090	6799	-0.205

and the total. For each rain type and the total, three N_0 - W diagnostic relations derived using different methods are presented. Stratiform, mixed, and convective rain account for 47% (35,752), 49% (37,369), and 4% (2,857) of the total data (75,978), respectively. The estimated N_0 mostly ranges within 864–83,837 $\text{m}^{-3} \text{mm}^{-1}$ for total, 1,180–85,012 $\text{m}^{-3} \text{mm}^{-1}$ for stratiform rain, 731–84,152 $\text{m}^{-3} \text{mm}^{-1}$ for mixed rain, and 706–29,142 $\text{m}^{-3} \text{mm}^{-1}$ for convective rain, where the

numbers are the 1st and 99th percentiles. For each of the total and three rain types, N_0 diagnosed by DNW and DMM stays within the 1st–99th percentile range of estimated N_0 for a wide range of W , while N_0 diagnosed by DNL stays within this range for only a limited range of W . The diagnostic relations derived from the same method show a consistent tendency for the different rain types and total. In DNW, N_0 increases as W increases, but in DNL and DMM, N_0

Fig. 3 Density scatter plots of the intercept parameter N_0 and the rainwater content W estimated from the disdrometer data for **a** total, **b** stratiform rain, **c** mixed rain, and **d** convective rain. The solid, dotted, and dashed lines indicate DNW, DNL, and DMM, respectively. The gray shaded area represents the range between the 1st and 99th percentiles of N_0



decreases as W increases. The exponent values of the diagnostic relations show that the slope of the diagnostic relation derived from each method is steeper for the individual rain types than for the total data. For example, DNW has an exponent value of 0.071 for the total data, which indicates a very weak dependency of N_0 on W , while it has larger values of exponent (0.327, 0.746, and 0.365 for stratiform, mixed, and convective rain, respectively) for individual rain types. This indicates that using different diagnostic relations according to the rain type improves the representation of the dependency of N_0 on W .

Depending on the method used to derive the diagnostic relation, the rain type that shows the largest variation of diagnosed N_0 changes. For example, for DNW and DNL, the largest variation of diagnosed N_0 appears in mixed rain, while it appears in stratiform rain for DMM. According to Tokay and Short (1996), the rain rate range of 1–10 mm h⁻¹ is the range where convective and stratiform rain occur in similar frequency so that the N_0 jump is most important, which indicates that the N_0 variation is large for this rain rate range. Given that this rain rate range is classified as mixed rain in this study, DNW and DNL well reflect the characteristics of mixed rain. In addition, Tokay and Short (1996) showed that N_0 increases when W increases for the rain rate of 5 mm h⁻¹, and only DNW shows an increasing tendency of diagnosed N_0 with W for mixed rain.

To further evaluate the diagnostic relations, the density scatter plots of N_0 diagnosed from the diagnostic relations against N_0 estimated from the disdrometer data are plotted (Fig. 4). In Fig. 4a–c, the diagnosed N_0 obtained without the rain-type classification is compared to the estimated N_0 . N_0 diagnosed by DNW and DMM is concentrated near 8,000 m⁻³ mm⁻¹, which is the value of N_0 of the Marshall-Palmer distribution. The standard deviations of the N_0 diagnosed by DNW and DMM are relatively small (523 and 1,189 m⁻³ mm⁻¹, respectively) compared to that of estimated N_0 (16,803 m⁻³ mm⁻¹). As a result, the correlation coefficient R is close to zero for both diagnostic relations, indicating that DNW and DMM without the rain-type classification can hardly reproduce the variation of the estimated N_0 . On the other hand, the standard deviation of the N_0 diagnosed by DNL is 18,082 m⁻³ mm⁻¹, similar to that of estimated N_0 . However, R is negative, showing DNL's poor capability of reproducing the estimated N_0 .

In Fig. 4d–f, the diagnosed N_0 obtained with the rain-type classification is compared to the estimated N_0 . Compared to the diagnosed N_0 obtained without the rain-type classification, that obtained with the rain-type classification shows larger standard deviations of diagnosed N_0 , which are 2,401, 5.709 × 10⁸, and 1,624 m⁻³ mm⁻¹ for DNW, DNL, and DMM, respectively. For N_0 diagnosed by DNW, R increases from 0.08 to 0.24 as the rain-type classification is considered (Fig. 4a and d). The rain-type classification makes it possible

to diagnose a wider range of N_0 . For N_0 diagnosed by DNL, R is still negative despite the consideration of the rain-type classification (Fig. 4b and e). In addition, DNL with the rain-type classification yields too much dispersion of diagnosed N_0 . Because DNL without the rain-type classification already diagnoses a sufficiently wide range of N_0 , the rain-type classification causes DNL to diagnose an unrealistically wide range of N_0 . For N_0 diagnosed by DMM, the diagnosed and estimated N_0 become even more negatively correlated when the rain-type classification is applied to the diagnostic relation (Fig. 4c and f).

In Fig. 4g–i, the diagnosed N_0 using the diagnostic relations of the previous studies (Z08 and AB12) is compared to the estimated N_0 . Z08 derived DNW ($N_0 = 24144 W^{1.326} \text{ m}^{-3} \text{ mm}^{-1}$) and DMM ($N_0 = 7106 W^{0.648} \text{ m}^{-3} \text{ mm}^{-1}$) using the RSD data of summertime rainfall in Oklahoma, and AB12 derived DNL ($N_0 = 3018 W^{-1.222} \text{ m}^{-3} \text{ mm}^{-1}$) using the RSD data collected from various field campaigns and disdrometer observations around the world. When applied to diagnose N_0 in South Korea, DNW and DMM of Z08 overall underdiagnose N_0 , whereas DNL of AB12 overdiagnoses N_0 . All the three diagnostic relations of the previous studies show R close to zero, suggesting that a diagnostic relation obtained using the RSD data of one region may not perform well in another region. In other words, to improve precipitation prediction of a numerical model in one region, a diagnostic relation that is derived using the RSD data of that region should be applied.

Based on the evaluation of different diagnostic relations so far, DNW with the rain-type classification is selected as the diagnostic relation to be implemented into a single-moment microphysics scheme in a numerical model to improve precipitation prediction. The reasons are as follows: (1) With or without the rain-type classification, N_0 diagnosed by DNL and DMM are negatively correlated with the estimated N_0 , which means that they have a tendency to diagnose N_0 inversely. (2) The rain-type classification improves the capability of DNW to reproduce the wide range of estimated N_0 and strengthens the correlation between the diagnosed and estimated N_0 .

3 Impacts of the Derived Diagnostic Relation on Precipitation Prediction

3.1 Model Description and Simulation Setup

The Weather Research and Forecasting (WRF) model version 4.2 (Skamarock et al. 2019) is used in this study. Figure 5 shows the model domain configuration. Three one-way nested domains centered on South Korea are considered. The horizontal grid spacings (numbers) of domains 1, 2, and 3 are 27 (150 × 120), 9 (217 × 184), and 3 km (253 × 244), respectively.

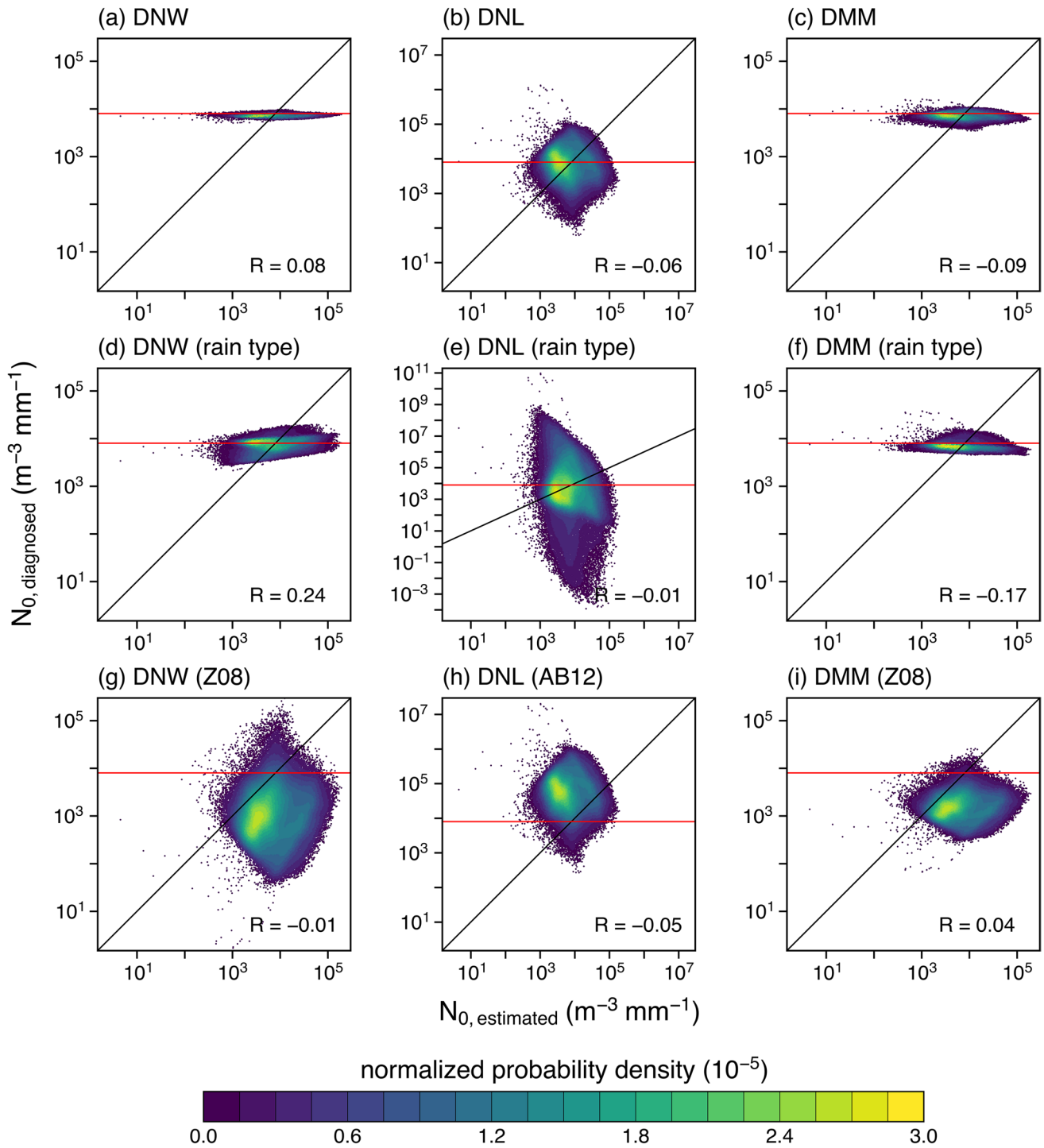


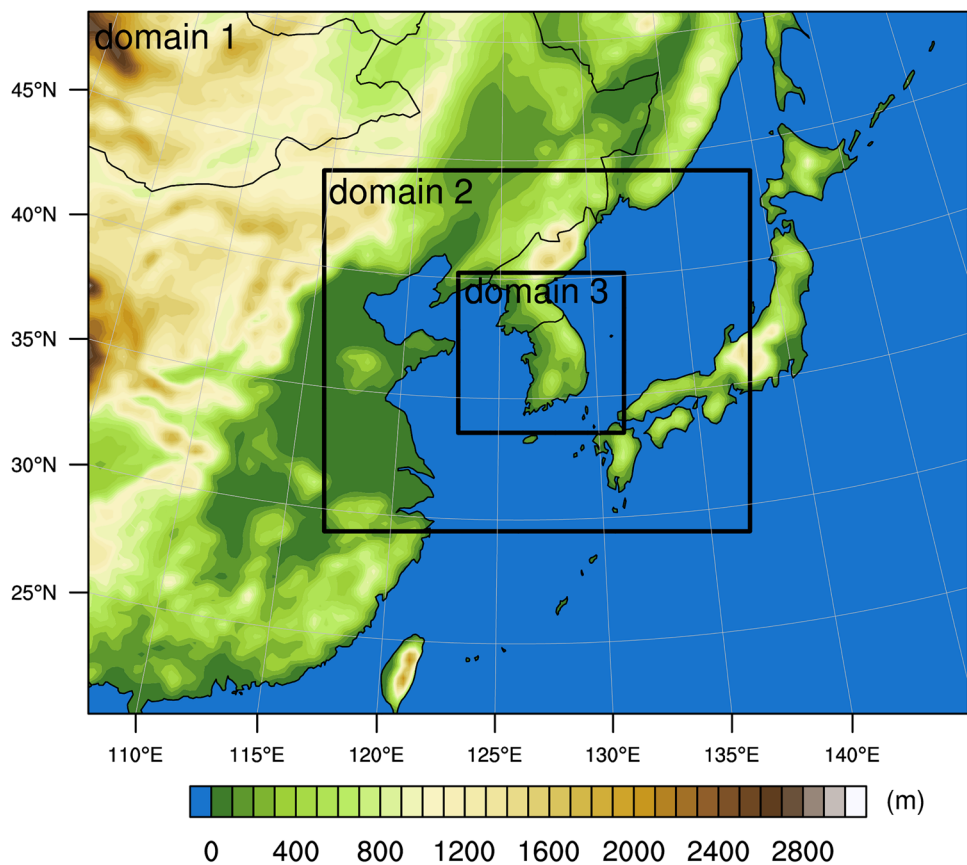
Fig. 4 Density scatter plots of the intercept parameter estimated from the disdrometer data, $N_0, \text{estimated}$, and the intercept parameter diagnosed from the diagnostic relations, $N_0, \text{diagnosed}$, for different diagnostic relations **a–c** derived without the rain-type classification, **d–f** derived with the rain-type classification, and **g–i** provided by the

previous studies. The probability density is normalized by the maximum probability density. The black line represents the identity line, and the red line represents the value of N_0 of the Marshall-Palmer distribution (8,000 m⁻³ mm⁻¹). R in each subfigure stands for the correlation coefficient

For all domains, the number of vertical layers is 49 and the vertical grid spacing is stretched from ~60 m in the lowest layer to ~450 m in the highest layer. The height of the model

top is 50 hPa (~20 km). The fifth generation of reanalysis data from the European Centre for Medium-Range Weather Forecasts (ERA5, Hersbach et al. 2020) with 1-h temporal

Fig. 5 Model domain configuration. The shades represent the terrain height



resolution and $0.25^\circ \times 0.25^\circ$ horizontal resolution are used as initial and boundary conditions. The physical parameterizations used in this study are the WRF single-moment 6-class (WSM6) cloud microphysics scheme (Hong and Lim 2006), the Kain–Fritsch cumulus parameterization scheme (Kain 2004), the Yonsei University PBL scheme (Hong et al. 2006), the revised MM5 surface layer scheme (Jiménez et al. 2012), the unified Noah land surface model (Tewari et al. 2004), the Dudhia shortwave radiation scheme (Dudhia 1989), and the Rapid Radiative Transfer Model (RRTM) longwave radiation scheme (Mlawer et al. 1997). The cumulus parameterization scheme is not applied to the innermost domain.

The diagnostic relation for N_0 selected in Subsection 2.3 is implemented into the WSM6 cloud microphysics scheme. The diagnostic relation requires two information: the rain type and the rainwater content W . In this study, the rain type of any column where rainwater exists is determined by the surface rain rate if it is not zero or the rain rate at the lowest level at which rainwater exists if the surface rain rate is zero. The rain rate criteria used to determine the rain type are the same as those used for the rain-type classification in Subsection 2.3. W used in the diagnostic relation can be determined by two different ways. One way is to use W at each level (Option E). This gives different diagnoses of N_0 at different levels because W varies within a column. The other way is to use W at the lowest level of its presence

(Option L). In this way, a column is assigned a single value of N_0 . Because the two options are expected to cause some differences in precipitation prediction, they are both tested in the precipitation simulations in this study.

In this study, we simulate the precipitation events that occurred in South Korea during the 7-day period from 12 UTC 27 July to 12 UTC 3 August 2020 when the Changma front, a quasi-stationary front that forms during the East Asian summer monsoon, affected South Korea. The model is initialized every day at 00 UTC and integrated for 36 h, and the first 12 h is considered as a spin-up time. Three sets of simulations are conducted, one with the original WSM6 scheme (WSM6-O simulation) and the other two with the WSM6 scheme where the diagnostic relation for N_0 is implemented with Option E (WSM6-E simulation) and Option L (WSM6-L simulation), respectively. The analysis of the simulation results is done for the innermost domain.

3.2 Simulation Results

3.2.1 Evaluation of the Simulations with Different Methods of Applying the Diagnostic Relation

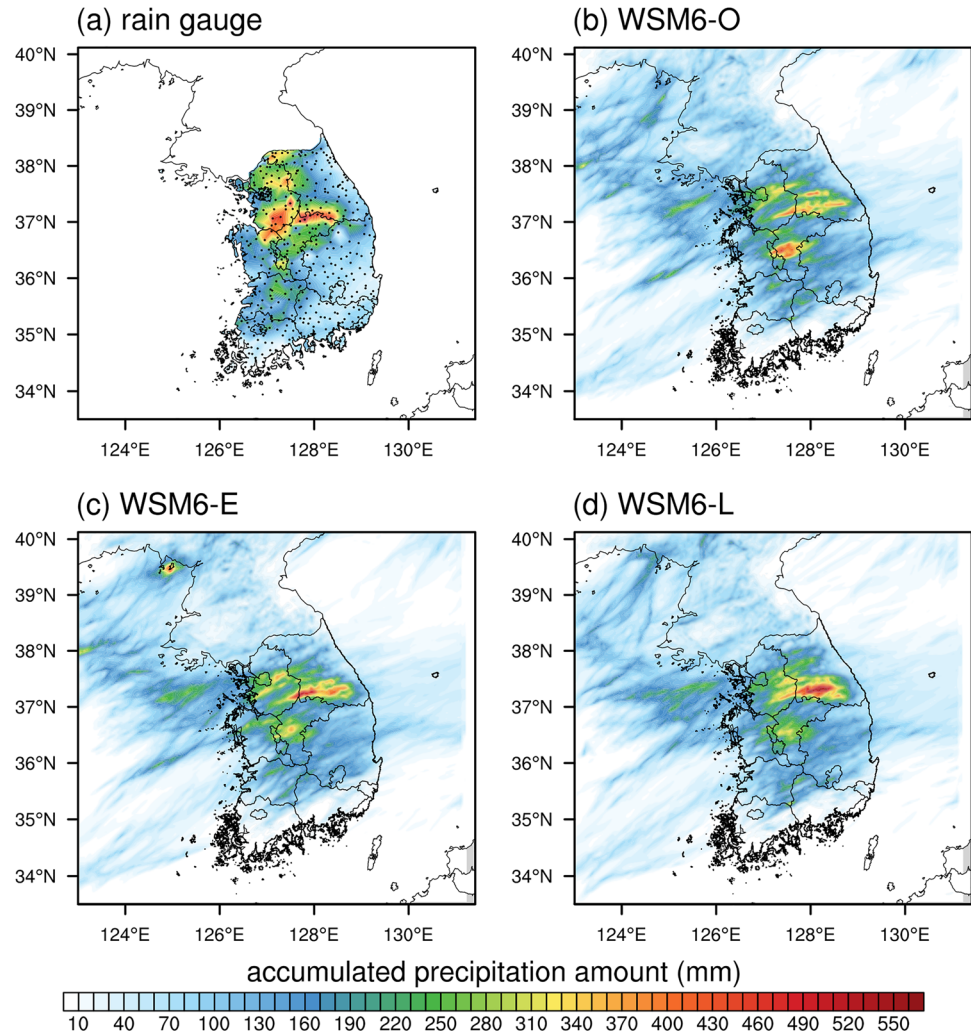
The 7-day precipitation amounts from rain gauge observation and predicted in the WSM6-O, WSM6-E, and WSM6-L simulations are shown in Fig. 6. For each set of simulations,

the 7-day accumulated precipitation amount is calculated by summing up the last 24-h accumulated precipitation amounts of the 7 simulations. During the 7-day period, a large amount of precipitation was observed in the region at $\sim 37^{\circ}\text{N}$ that is elongated in the west–east direction. The precipitation in the west part of this region is not predicted well in all three simulations. The precipitation in the east part of this region is predicted by the three simulations, but their predictions show large differences. The WSM6-O simulation predicts the precipitation in this region, but with a much smaller amount (local maximum: 415 mm) than the observed amount (local maximum: 569 mm). The maximum precipitation amount in the WSM6-O simulation (454 mm) is found further away to the south at $\sim 36.3^{\circ}\text{N}$, not in this region. The WSM6-E simulation predicts a larger amount of precipitation in this region (local maximum: 527 mm) compared to the WSM6-O simulation, but it is still smaller than the observation. The WSM6-L simulation predicts an even larger amount of precipitation in this region (local maximum: 566 mm), which is close to the observation.

To quantitatively compare the performances of the three simulations and select the better option for applying the diagnostic relation for N_0 to the WSM6 scheme, the root mean squared error (RMSE) and the correlation coefficient R are calculated. The WSM6-L simulation shows the smallest RMSE (89 mm), followed by the WSM6-O (91 mm) and WSM6-E (94 mm) simulations. Also, the WSM6-L simulation shows the highest value of R (0.62), followed by the WSM6-O (0.60) and WSM6-E (0.58) simulations. Applying the diagnostic relation for N_0 with Option L improves the precipitation prediction, while that with Option E degrades the precipitation prediction.

The WSM6-L simulation shows the best performance not only for the 7-day accumulated precipitation amount but also for individual daily precipitation amounts. RMSEs in the WSM6-O, WSM6-E, and WSM6-L simulations are 36, 36, and 34 mm, respectively, and R in these simulations are 0.45, 0.44, and 0.48, respectively. For the prediction of daily precipitation amounts, the performances of the WSM6-O and WSM6-E simulations are similar to each other. Also, when

Fig. 6 Seven-day accumulated precipitation amount **a** observed at 561 rain gauge stations (marked with black dots in **a**) and predicted in the **b** WSM6-O, **c** WSM6-E, and **d** WSM6-L simulations



the evaluation indices above are calculated based on hourly precipitation amounts, the WSM6-L simulation gives a smaller RMSE (4.61 mm) than the WSM6-O (4.64 mm) and WSM6-E (4.63 mm) simulations, and a higher value of R (0.17) than the two simulations (0.15 for both WSM6-O and WSM6-E). The equitable threat scores (ETSSs) calculated using daily precipitation amounts and hourly precipitation amounts are presented in Fig. 7a and b, respectively. Compared to the WSM6-O simulation, both ETSSs are improved for almost all precipitation amount thresholds in the WSM6-L simulation. In the WSM6-E simulation, however, ETSSs are improved only for a limited range of precipitation amount threshold (10–55 mm for daily precipitation amounts; 4–8 mm and 30–40 mm for hourly precipitation amounts) compared to the WSM6-O simulation. These results suggest that the impacts of applying the diagnostic relation for N_0 can be sensitive to how it is applied at upper levels where N_0 cannot be directly evaluated. Figuring out which option is more realistic at upper levels deserves investigation using RSD observation data at different altitudes, which cannot be done in this study. In this study, based on the quantitative evaluations for the simulated precipitation amounts at the surface, Option L is selected as the option for applying the diagnostic relation for N_0 to the WSM6 scheme.

3.2.2 Impacts of the Diagnostic Relation on Cloud Microphysical Characteristics

In this subsection, the WSM6-L simulation is compared with the WSM6-O simulation to examine the impacts of the diagnostic relation for N_0 on the prediction of cloud and precipitation characteristics. In Fig. 8, N_0 and Λ in the WSM6-O and WSM6-L simulations are evaluated in comparison with N_0 and Λ from the disdrometer observation. N_0 and Λ at the lowest level at the model grid points closest to each of the four disdrometer sites are compared to those estimated from the disdrometer data of the four sites during the seven-day period. The range between the 1st and 99th percentiles of predicted N_0 in the WSM6-L simulation is $2,583\text{--}13,542 \text{ m}^{-3} \text{ mm}^{-1}$. Although this range is narrower than that of the observed N_0 ($654\text{--}43,845 \text{ m}^{-3} \text{ mm}^{-1}$), the representation of N_0 is substantially improved compared to the WSM6-O simulation where N_0 is fixed at $8000 \text{ m}^{-3} \text{ mm}^{-1}$. Furthermore, the WSM6-L simulation predicts that the peak of PDF appears at $N_0 \sim 6000 \text{ m}^{-3} \text{ mm}^{-1}$, which is very close to the observation. The WSM6-O simulation predicts Λ in a much broader range compared to the observation. Especially, the WSM6-O simulation predicts the occurrence of Λ greater than 9 mm^{-1} which does not appear in the observation. In the WSM6-L simulation, the upper limit of simulated Λ decreases so that the PDF of simulated Λ becomes more similar to that of the observed Λ . However, discontinuities of PDF that does not

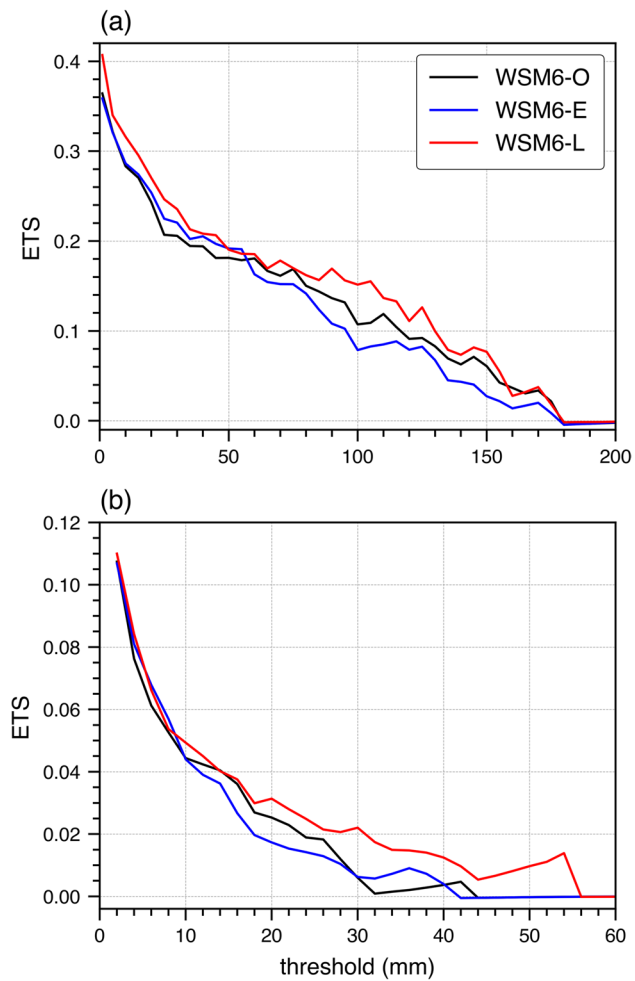
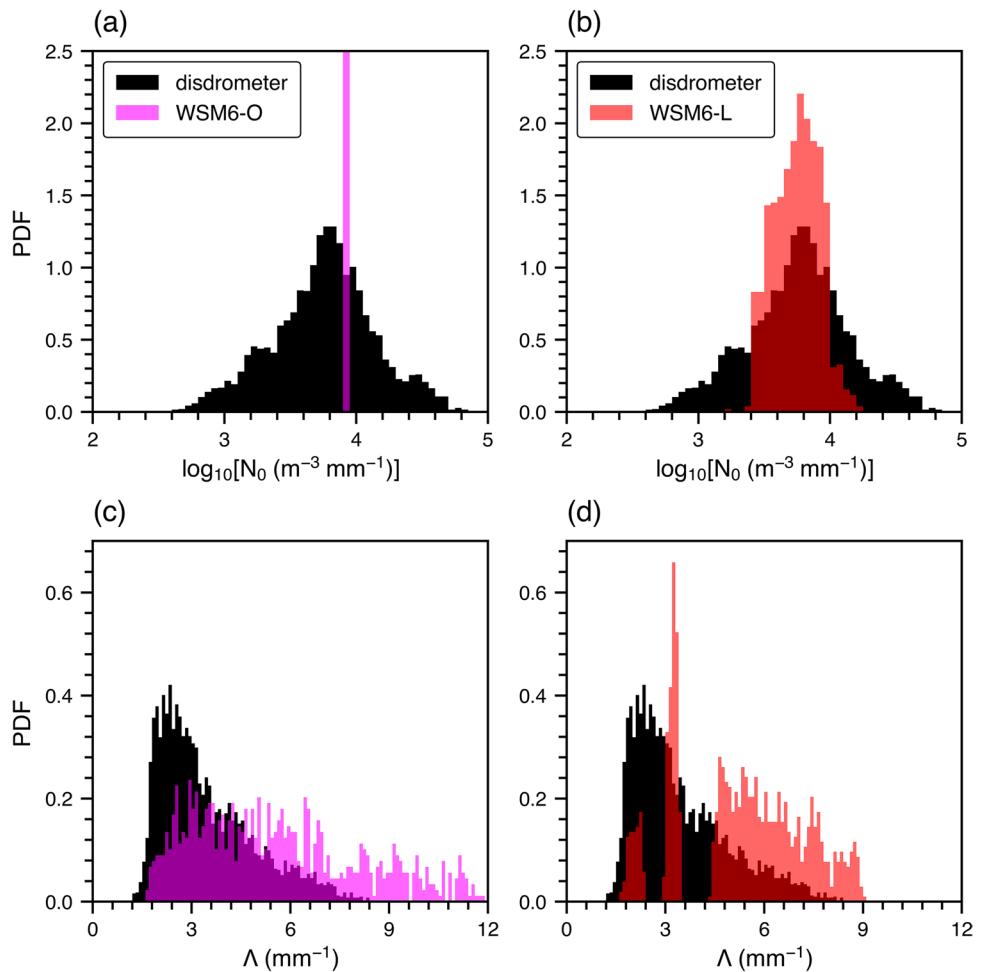


Fig. 7 Equitable threat scores for **a** daily precipitation amounts and **b** hourly precipitation amounts in the WSM6-O, WSM6-E, and WSM6-L simulations

appear in the observation appear at Λ ranges of $2.4\text{--}3.0$ and $3.6\text{--}4.2 \text{ mm}^{-1}$. This is caused by the rain-type classification in the diagnostic relation. The left, middle, and right parts of the Λ PDF in the WSM6-L simulation are from convective, mixed, and stratiform rain, respectively, in this simulation.

The vertical profiles of $\log_{10}N_0$ and Λ in the WSM6-O and WSM6-L simulations are compared in Fig. 9, where N_0 and Λ are time- and domain-averaged. The average N_0 in the WSM6-L simulation is smaller than that in the WSM6-O simulation at almost all heights, up to ~ 8.5 km. The difference in the average N_0 is prominent below $z \sim 4.5$ km, and N_0 at these levels is $2,846 \text{ m}^{-3} \text{ mm}^{-1}$ on average in the WSM6-L simulation. The WSM6-L simulation also shows smaller average Λ compared to the WSM6-O simulation. The average Λ below $z = 4.5$ km is 10.1 mm^{-1} in the WSM6-L simulation and 15.9 mm^{-1} in the WSM6-O simulation. Because the average W in the WSM6-L simulation is almost the same as that in the WSM6-O simulation (not shown), the

Fig. 8 Probability density functions (PDFs) for **a, b** the logarithm of the intercept parameter N_0 and **c, d** the slope parameter Λ estimated from the disdrometer data and obtained from the **a, c** WSM6-O and **b, d** WSM6-L simulations



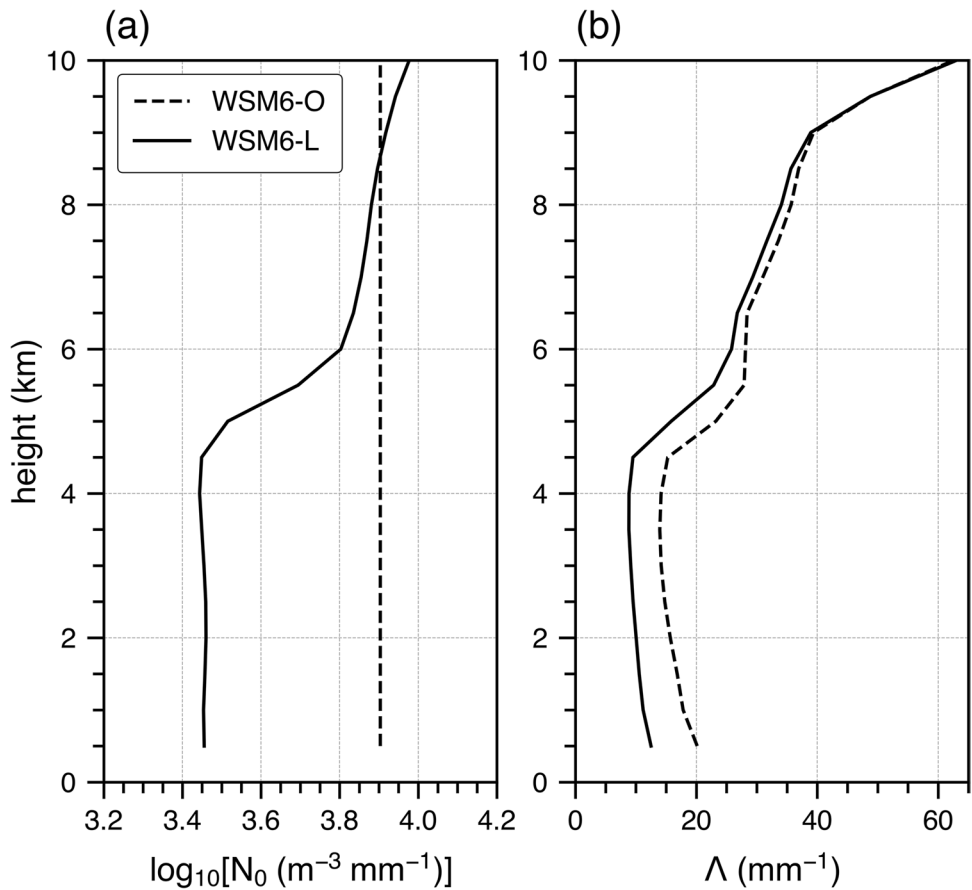
relatively small average N_0 and Λ in the WSM6-L simulation suggest that on average, the RSD in the WSM6-L simulation consists of a larger number of large-size raindrops and a smaller number of small-size raindrops than the RSD in the WSM6-O simulation.

Figure 10 presents the time- and domain-averaged vertical profiles of the hydrometeor mixing ratios obtained from the WSM6-O and WSM6-L simulations and their differences. In both simulations, the proportion of the mixing ratio of each hydrometeor to the total is almost the same (Fig. 10a and b). In both simulations, the mixing ratio of snow accounts for the largest proportion of 35% to the total and the sum of the mixing ratios of ice hydrometeors accounts for 69% of the total. This indicates that ice microphysical processes are highly involved. The rainwater mixing ratios in both simulations have almost identical vertical profiles that show a peak at $z=3.5$ km. Compared to the WSM6-O simulation, the rainwater mixing ratio in the WSM6-L simulation is smaller at almost all levels, overall by 3%. The reduction of the rainwater mixing ratio is largest at $z=4$ km, below the melting layer. The WSM6-L simulation also shows smaller cloud water mixing ratio except for below $z\sim 2$ km. The cloud

ice mixing ratio is slightly larger at $z\sim 5\text{--}8$ km and smaller above $z=8$ km in the WSM6-L simulation. The WSM6-L simulation shows smaller snow mixing ratio at almost all levels, overall by 3%, and smaller graupel mixing ratio at $z\sim 4\text{--}8$ km.

Figure 11 shows the time- and domain-averaged vertical profiles of microphysical conversion rates related to rainwater obtained from the WSM6-O and WSM6-L simulations and their differences. Note that Fig. 11a–c and d–f represent the source terms and sink terms of rainwater mass, respectively. The two simulations have the similar vertical profiles of microphysical conversion rates. Among the microphysical processes, the melting of ice hydrometeors contributes most to the rainwater production. In both simulations, the rate of melting of ice hydrometeors is ~ 10 times the rate of accretion of cloud water, when the rates are vertically integrated. The rates of melting of snow and graupel are both greatest at $z=4.5$ km. Except for the melting of ice hydrometeors, the accretion of cloud water by rainwater is the largest source of rainwater mass, followed by the autoconversion of cloud water. The conversion rates for source processes related to cloud water (PRAUT, PRACW, and PAACW) are

Fig. 9 Vertical profiles of **a** the logarithm of the intercept parameter N_0 and **b** the slope parameter Λ . N_0 and Λ are time- and domain-averaged



greatest at $z=4.5$ km where the peak of cloud water mixing ratio appears (Fig. 10a and b). The largest sink of rainwater mass is rainwater evaporation, which is most active at $z\sim 2.5\text{--}3$ km. The accretion of rainwater by ice hydrometeors and freezing occur near or above the melting layer, but the conversion rates for those processes are much smaller than the evaporation rate. The WSM6-L simulation shows overall 4% smaller rate of accretion of cloud water and 3% smaller melting rates of snow and graupel than the WSM6-O simulation (Fig. 11c). The evaporation rate in the WSM6-L simulation is overall 7% smaller than that in the WSM6-O simulation (Fig. 11f). The decreases in the rates of accretion and melting contribute to the decrease in rainwater mixing ratio in the WSM6-L simulation, and the contribution of the latter is larger.

Overall, the implementation of the N_0 diagnostic relation causes decreases in the rates of evaporation, accretion of cloud water, and melting. Because of the diagnostic relation, the WSM6-L simulation predicts N_0 that is on average smaller than the prescribed value in the WSM6-O simulation, which to some extent agrees with the observation that the peak of N_0 PDF appears at the value that is smaller than the prescribed value (Fig. 8). The smaller number of small raindrops and larger number of large raindrops in the RSDs in the WSM6-L simulation caused by the smaller N_0 and

Λ decrease the evaporation rate due to the smaller surface area and faster sedimentation of raindrops on average. The reduced evaporative cooling can affect the thermodynamic environment and lead to some changes in convection development. Figure 12 shows the differences in the horizontal fields and vertical profiles of virtual potential temperature θ_v between the WSM6-L and WSM6-O simulations. At $z=4$ km where the decrease in rainwater evaporation in the WSM6-L simulation is maximized (Fig. 11f), θ_v is higher in the WSM6-L simulation over most of the domain due to the reduced evaporative cooling (Fig. 12a). At $z=1$ km, on the other hand, θ_v is lower in the WSM6-L simulation over most of the domain (Fig. 12b). Consequently, the thermodynamic environment in the WSM6-L simulation is more stable than that in the WSM6-O simulation (Fig. 12c), which can lead to reduced cloud activities and thus the reduced amount of condensates in the WSM6-L simulation (Fig. 10c).

When the rainwater mixing ratio is not changed much, a decrease in N_0 and the corresponding decrease in Λ result in a decrease of accretion rate, based on the formula of the WSM6 scheme where the accretion rate is proportional to $N_0/\Lambda^{3.8}$ (Eq. (A40) in Hong et al. (2006)). The faster sedimentation of raindrops in the WSM6-L simulation can decrease the upward transport of raindrops above the freezing level, which can weaken ice microphysical processes.

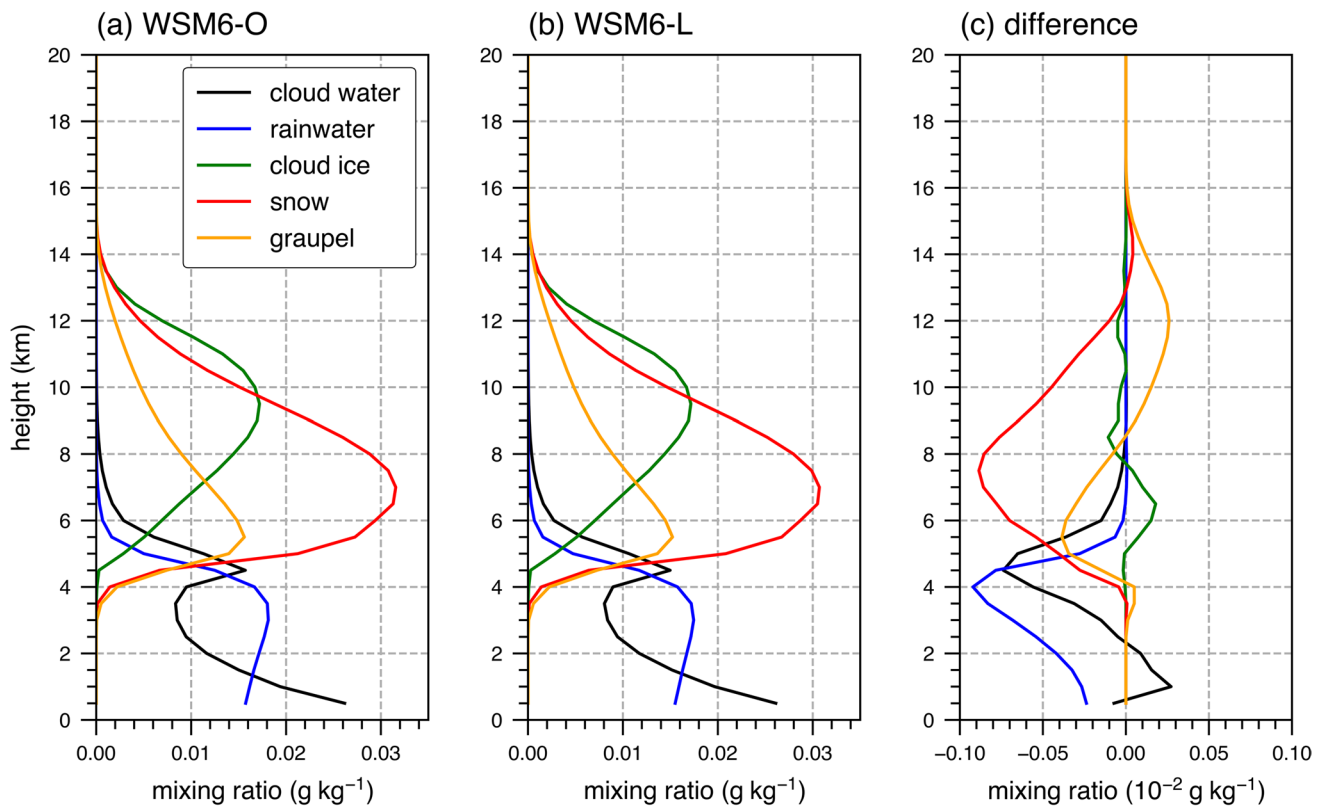


Fig. 10 Time- and domain-averaged vertical profiles of hydrometeor mixing ratios obtained from the **a** WSM6-O and **b** WSM6-L simulations and **c** their differences (WSM6-L minus WSM6-O)

This may be a possible reason for the decreases in the ice hydrometeor mixing ratios and thus the decreases in the rates of melting of snow and graupel in the WSM6-L simulation.

The impacts of applying the diagnostic relation for N_0 on precipitation prediction can to some extent vary depending on the precipitation case. In addition to the summertime precipitation case analyzed above, a precipitation case associated with a low pressure system that occurred in April is simulated. The simulation period is from 06 UTC 2 to 18 UTC 3 April 2021, and the last 24 h of the period is the analysis period. Figure 13 shows 24-h accumulated precipitation amount from rain gauge observation and predicted in the WSM6-O and WSM6-L simulations. The WSM6-L simulation shows smaller RMSE (11.4 mm) and higher R (0.85) than the WSM6-O simulation (RMSE: 11.6 mm, R : 0.84) as in the summertime precipitation case, but the difference in the performance between the two simulations are reduced. The simulated N_0 and Λ are evaluated in Fig. 14, and the WSM6-L simulation still shows its advantages, that is, better predicting N_0 than the WSM6-O simulation and preventing the appearance of unrealistically high Λ . In the vertical profiles of hydrometeor mixing ratios (Fig. 15), the WSM6-L simulation shows smaller rainwater mixing ratio and snow mixing ratio than the WSM6-O simulation, which is also seen for the summertime precipitation case. On the other

hand, the change in cloud water mixing ratio is not consistent in the two cases, which indicates that the impacts of the diagnostic relation on cloud microphysical characteristics can change with the precipitation case to some extent.

For the two precipitation cases simulated in this study, improvements in precipitation prediction are seen. More rigorous evaluation of the impacts of the diagnostic relation can be conducted if a larger variety of precipitation cases are simulated, which may be done in the future when more computational resources are available.

4 Summary and Conclusions

In this study, we derived the diagnostic relations for the intercept parameter of the exponential raindrop size distribution N_0 for different rain types (stratiform, mixed, and convective) using the disdrometer data and examined the impacts of the diagnostic relations on precipitation prediction. The disdrometer data observed at four sites (Seoul, Chuncheon, Jincheon, and Boseong) in South Korea show spatiotemporal variations of N_0 . The diagnostic relations derived using three different methods (DNW, DNL, DMM) with and without the rain-type classification are evaluated,

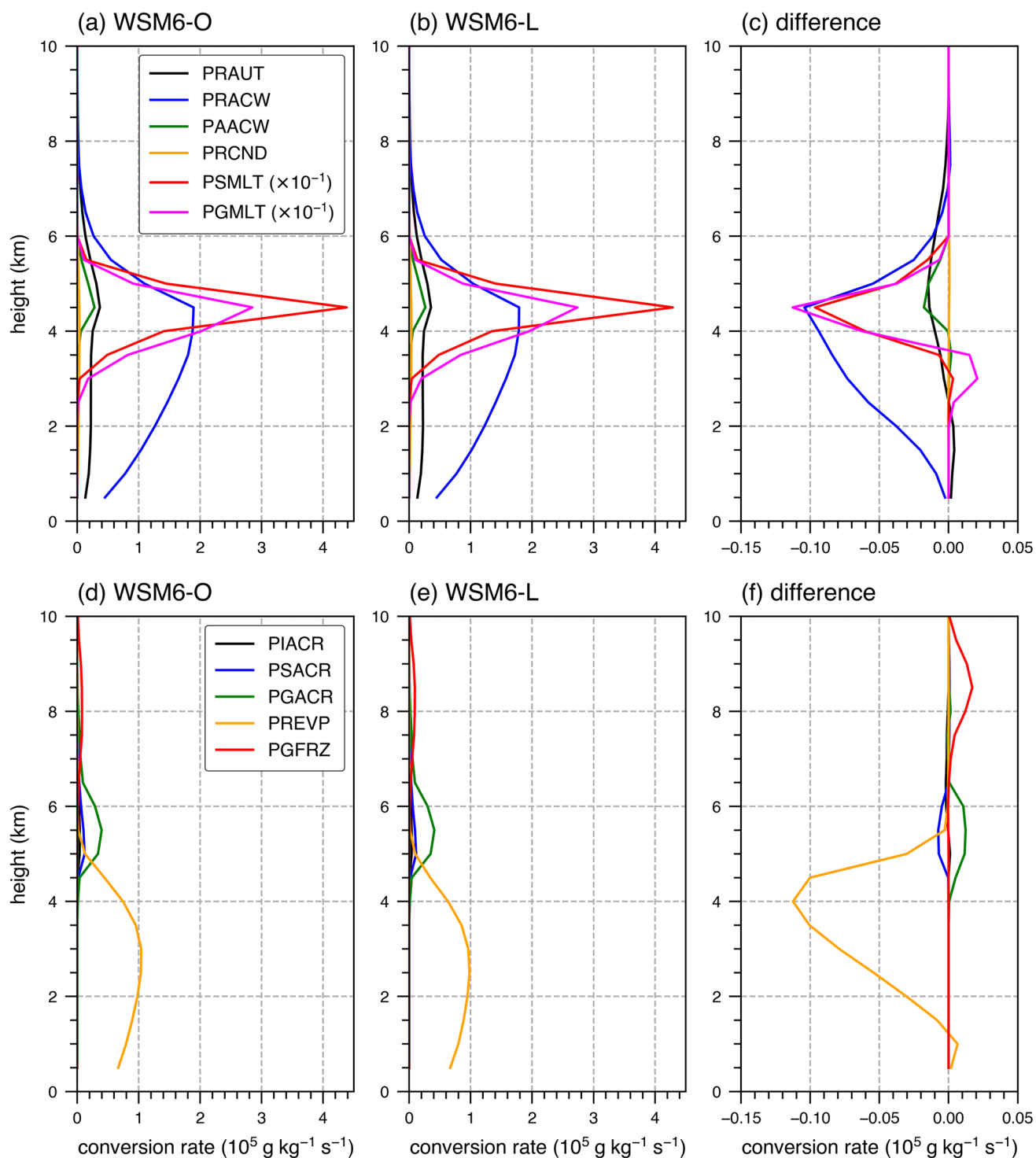


Fig. 11 Time- and domain-averaged vertical profiles of microphysical conversion rates related to rainwater (PRAUT: autoconversion of cloud water to rainwater, PRACW: accretion of cloud water by rainwater, PAACW: weighted mean of two types of accretion – accretion of cloud water by snow and accretion of cloud water by graupel, PRCND: condensation on rainwater, PSMLT: snow melting, PGMLT:

graupel melting, PIACR: accretion rate of rainwater by cloud ice, PSACR: accretion rate of rainwater by snow, PGACR: accretion rate of rainwater by graupel, PREVP: evaporation of rainwater, PGFRZ: freezing of rainwater) obtained from the **a**, **d** WSM6-O and **b**, **e** WSM6-L simulations and **c**, **f** their differences (WSM6-L minus WSM6-O)

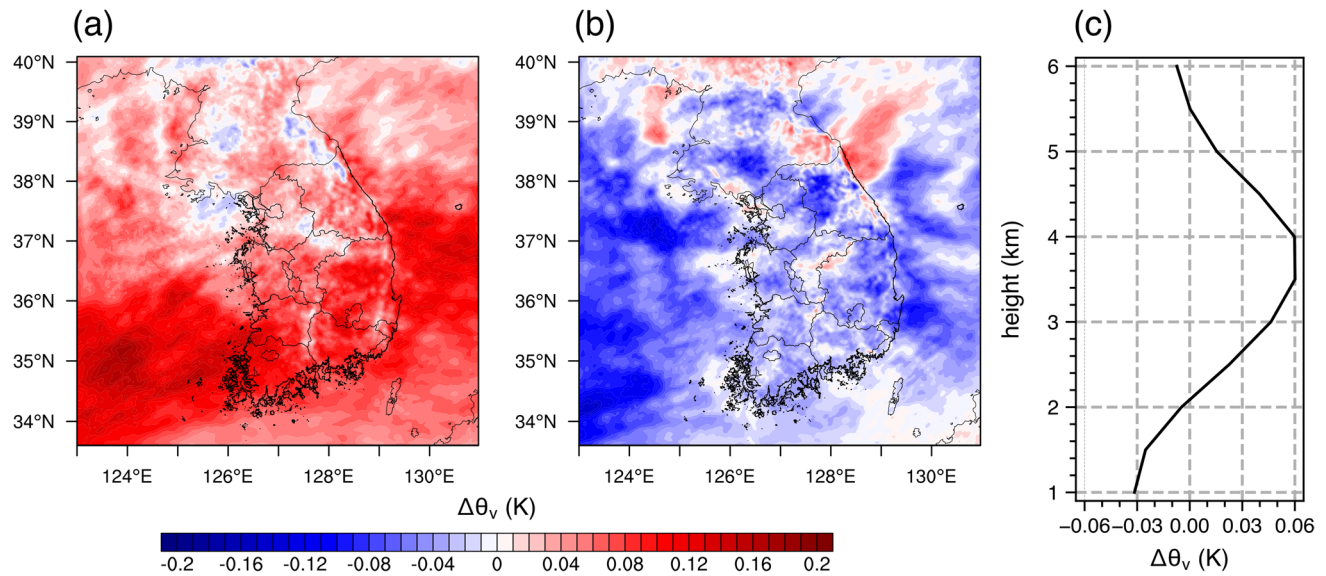


Fig. 12 Differences in the horizontal fields at **a** $z=4\text{ km}$ and **b** $z=1\text{ km}$ and **c** vertical profiles of virtual potential temperature θ_v between the WSM6-L and WSM6-O simulations (WSM6-L minus WSM6-O)

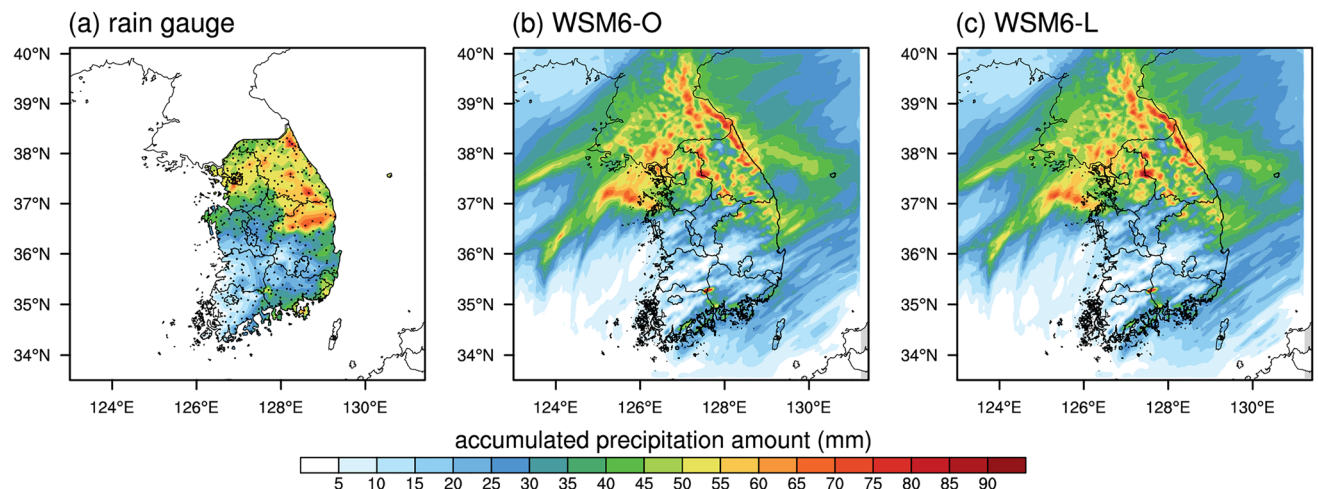


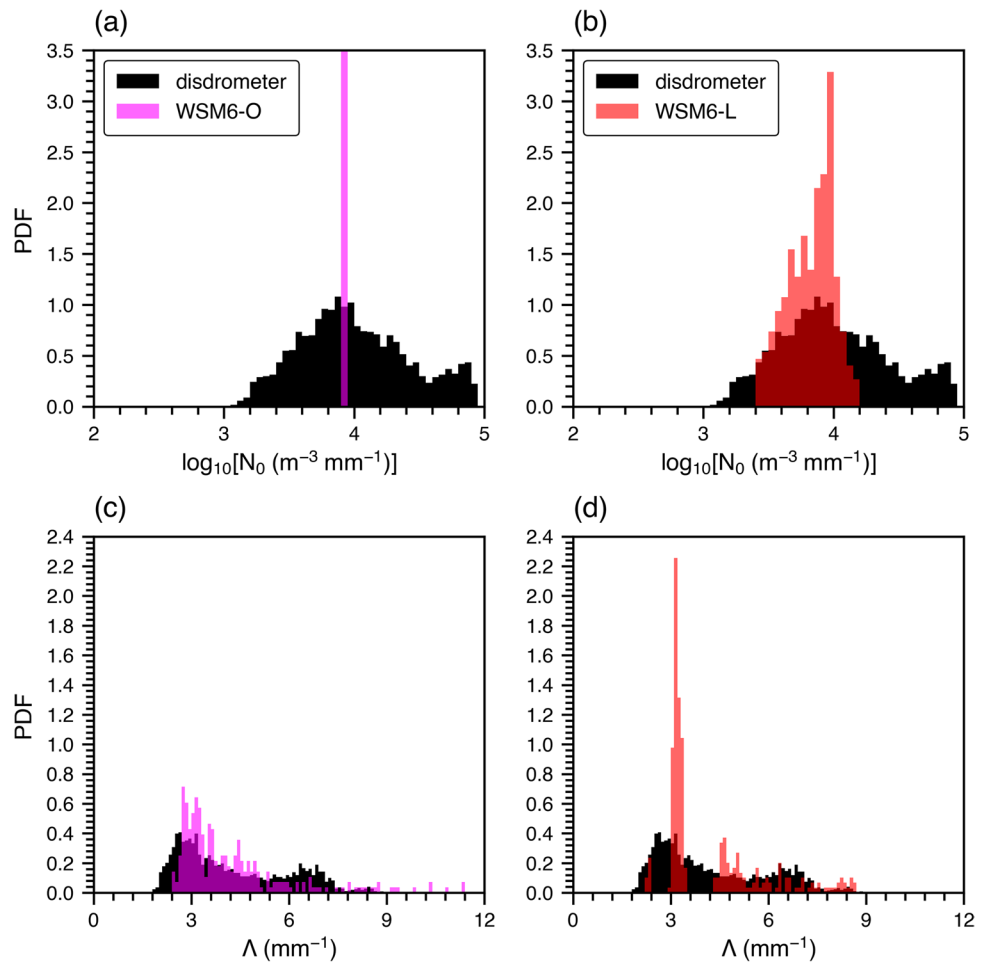
Fig. 13 24-h accumulated precipitation amount **a** observed at rain gauge stations (marked with black dots in **a**) and predicted in the **b** WSM6-O and **c** WSM6-L simulations

and DNW with the rain-type classification, which best reproduces the observed N_0 , is selected. DNW is implemented into the WSM6 scheme, and its impacts are investigated through the simulations of summertime precipitation events in South Korea. Compared to the WSM6-O simulation using a constant N_0 , the WSM6-L simulation using the diagnostic relation yields better precipitation prediction. The diagnostic relation greatly improves the representation of N_0 , which is observed to have a large variability. Also, the WSM6-L simulation predicts N_0 that is on average smaller than the prescribed value in the WSM6-O simulation, which agrees with the observation

to some extent. The smaller N_0 in the WSM6-L simulation decreases the rainwater mixing ratio by reducing the accretion of cloud water and the melting of ice hydrometeors and also decreases the rainwater evaporation.

We confirmed the potential of the use of diagnostic relation for N_0 in a single-moment microphysics scheme for better precipitation prediction. However, the advantage of using the diagnostic relation may be more prominent if the dependence of microphysical processes on varying N_0 is well represented in their parameterizations in the single-moment microphysics scheme. For example, when two exponential RSDs have the same rainwater content but different N_0 , it is

Fig. 14 As in Fig. 8, but for the precipitation case on 2–3 April 2021



generally expected that the rate of accretion of cloud water is larger for the RSD with smaller N_0 that has a larger number of large-size raindrops and a smaller number of small-size raindrops because the collection efficiency between raindrops and cloud droplets is higher for large raindrops than for small raindrops. However, the accretion rate in the WSM6 microphysics scheme is designed to decrease as N_0 decreases because it uses the collection efficiency that does not depend on the raindrop size. If the dependence of the accretion rate on the RSD properties is represented as in either simple (Thompson et al. 2008) or sophisticated (Ahmed et al. 2020) way, the impact of diagnostic relation may be more pronounced.

The appropriate diagnostic relation for N_0 for one region can be different from that for another region. DNW in this study and DNW of Z08 were derived using the same derivation method, but DNW in this study better reproduced the observed N_0 in South Korea because the relation was derived using the disdrometer data in South Korea. The diagnostic relation of AB12 also showed poor performance in reproducing N_0 in South Korea although it was derived using RSD data from various regions around the world. This indicates

that to make the best use of diagnostic relation for N_0 in predicting precipitation in a region, it is encouraged to use the diagnostic relation derived from that region. Ideally, for global weather prediction models, a set of diagnostic relations for different regions can be developed and employed in the model to improve precipitation prediction.

Although the diagnostic relation for N_0 that considers the rain-type classification shows stronger correlation between the estimated and diagnosed N_0 than the diagnostic relation that does not consider the rain-type classification, the correlation coefficient is 0.24, which means that a large part of the N_0 variation is not represented by the rainwater content and the rain type only. It can be expected that RSD can vary depending on the cloud characteristics such as the dominant microphysical process (Dolan et al. 2018) and the stage of cloud development, but it is not easy to establish a sophisticated diagnostic relation for N_0 utilizing those factors because it needs three-dimensional observations of RSD and in-cloud environment for various types of clouds, which is not available for now. In a future study, extensive numerical simulations of various types of clouds using a bin microphysics scheme may be done to obtain reliable

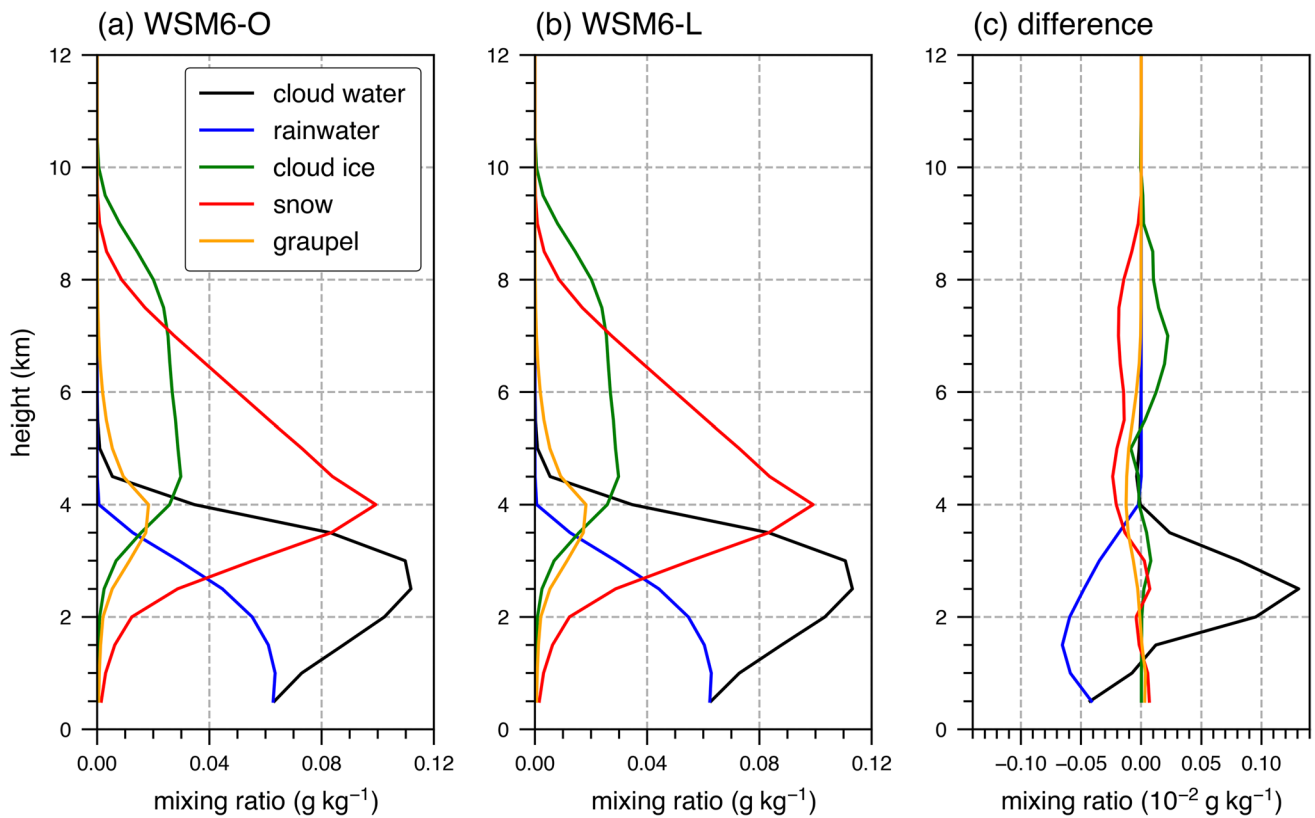


Fig. 15 As in Fig. 10, but for the precipitation case on 2–3 April 2021

three-dimensional RSD data and in-cloud environment data at the same time, which can be used to establish a more sophisticated diagnostic relation for N_0 that better represents the variation of N_0 .

In this study, the diagnostic relation derived with the rain-type classification performed better in reproducing the observed N_0 than that derived without the rain-type classification. There are various diagnostic relations other than the diagnostic relation for N_0 that are developed to use in bulk microphysics schemes, but the rain-type classification is not considered in most of them. Future studies may consider improving those diagnostic relations by including the rain-type classification as done in this study for the diagnostic relation for N_0 . For example, the shape parameter–slope parameter relationship for RSD used in some two-moment microphysics schemes (e.g., Cao et al. 2008) can be re-derived for different rain types, which is expected to improve the representation of RSD in various environments.

The usefulness of the diagnostic relation for N_0 that improves the single-moment scheme's ability to represent RSD may be little if double-moment schemes provide reliable predictions of RSD. However, there are some studies showing that current double-moment schemes have difficulties in reproducing RSDs in reality. For example, it was

reported that the WRF double-moment six-class (WDM6) microphysics scheme (Lim and Hong 2010) overestimates raindrop number concentration (Lei et al. 2020) and gives much higher values of the intercept parameter in the gamma size distribution than the disdrometer observations (Yang et al. 2019). Chen et al. (2021) evaluated D_m and $\log_{10}N_w$ simulated using three different double-moment schemes (Morrison et al. 2005; Milbrandt and Yau 2005; Thompson et al. 2008) for a Meiyu-front rainfall event against radar and disdrometer observations and showed that the simulated D_m and $\log_{10}N_w$ at low levels are overestimated and underestimated, respectively. In addition, when we tested a double-moment microphysics scheme for the summertime precipitation case analyzed above, it failed to reproduce the observed distribution N_0 , showing worse prediction of N_0 than the WSM6 scheme with the diagnostic relation for N_0 for this particular case (not shown). Extensive evaluation on the reliability of multi-moment microphysics schemes in RSD prediction can be an interesting topic for a future study.

Acknowledgements The authors are grateful to two anonymous reviewers for providing valuable comments on this work. This work was supported by the Korea Meteorological Administration Research and Development Program under Grant KMI 2020–00710 and also by the National Research Foundation of Korea (2021R1A2C1007044).

Open Access This article is licensed under a Creative Commons Attribution 4.0 International License, which permits use, sharing, adaptation, distribution and reproduction in any medium or format, as long as you give appropriate credit to the original author(s) and the source, provide a link to the Creative Commons licence, and indicate if changes were made. The images or other third party material in this article are included in the article's Creative Commons licence, unless indicated otherwise in a credit line to the material. If material is not included in the article's Creative Commons licence and your intended use is not permitted by statutory regulation or exceeds the permitted use, you will need to obtain permission directly from the copyright holder. To view a copy of this licence, visit <http://creativecommons.org/licenses/by/4.0/>.

References

- Abel, S.J., Boutle, I.A.: An improved representation of the raindrop size distribution for single-moment microphysics schemes. *Q. J. R. Meteorol. Soc.* **138**, 2151–2162 (2012)
- Ahmed, T., Jin, H.-G., Baik, J.-J.: A physically based raindrop–cloud droplet accretion parametrization for use in bulk microphysics schemes. *Q. J. R. Meteorol. Soc.* **146**, 3368–3383 (2020)
- Bringi, V.N., Chandrasekar, V., Hubbert, J., Gorgucci, E., Randeu, W.L., Schoenhuber, M.: Raindrop size distribution in different climatic regimes from disdrometer and dual-polarized radar analysis. *J. Atmos. Sci.* **60**, 354–365 (2003)
- Cao, Q., Zhang, G., Brandes, E., Schuur, T., Ryzhkov, A., Ikeda, K.: Analysis of video disdrometer and polarimetric radar data to characterize rain microphysics in Oklahoma. *J. Appl. Meteorol. Climatol.* **47**, 2238–2255 (2008)
- Chen, B., Yang, J., Gao, R., Zhu, K., Zou, C., Gong, Y., Zhang, R.: Vertical variability of the raindrop size distribution in typhoons observed at the Shenzhen 356-m meteorological tower. *J. Atmos. Sci.* **77**, 4171–4187 (2020)
- Chen, G., Zhao, K., Huang, H., Yang, Z., Lu, Y., Yang, J.: Evaluating simulated raindrop size distributions and ice microphysical processes with polarimetric radar observations in a Meiyu front event over eastern China. *J. Geophys. Res. Atmos.* **126**, e2020JD034511 (2021)
- Dolan, B., Fuchs, B., Rutledge, S.A., Barnes, E.A., Thompson, E.J.: Primary modes of global drop size distributions. *J. Atmos. Sci.* **75**, 1453–1476 (2018)
- Dudhia, J.: Numerical study of convection observed during the Winter Monsoon experiment using a mesoscale two-dimensional model. *J. Atmos. Sci.* **46**, 3077–3107 (1989)
- Grabowski, W.W., Morrison, H., Shima, S.-I., Abade, G.C., Dziekan, P., Pawlowska, H.: Modeling of cloud microphysics: can we do better? *Bull. Am. Meteorol. Soc.* **100**, 655–672 (2019)
- Hersbach, H., Bell, B., Berrisford, P., Hirahara, S., Horányi, A., Muñoz-Sabater, J., et al.: The ERA5 global reanalysis. *Q. J. R. Meteorol. Soc.* **146**, 1999–2049 (2020)
- Hong, S.-Y., Lim, J.-O.J.: The WRF single-moment 6-class microphysics scheme (WSM6). *J. Korean Meteorol. Soc.* **42**, 129–151 (2006)
- Hong, S.-Y., Noh, Y., Dudhia, J.: A new vertical diffusion package with an explicit treatment of entrainment processes. *Mon. Weather Rev.* **134**, 2318–2341 (2006)
- Janapati, J., Seela, B.K., Reddy, M.V., Reddy, K.K., Lin, P.-L., Rao, T.N., Liu, C.-Y.: A study on raindrop size distribution variability in before and after landfall precipitations of tropical cyclones observed over southern India. *J. Atmos. Sol.-Terr. Phys.* **159**, 23–40 (2017)
- Jang, J., Lee, Y.H., Joo, S.: An intercomparison study between optimization algorithms for parameter estimation of microphysics in unified model: micro-genetic algorithm and harmony search algorithm. *J. Korean Inst. Intell. Syst.* **27**, 79–87 (2017)
- Jiménez, P.A., Dudhia, J., González-Rouco, J.F., Navarro, J., Montávez, J.P., García-Bustamante, E.: A revised scheme for the WRF surface layer formulation. *Mon. Weather Rev.* **140**, 898–918 (2012)
- Jwa, M., Jin, H.-G., Lee, J., Moon, S., Baik, J.-J.: Characteristics of raindrop size distribution in Seoul, South Korea according to rain and weather types. *Asia-Pacific J. Atmos. Sci.* **57**, 605–617 (2021)
- Kain, J.S.: The Kain–Fritsch convective parameterization: an update. *J. Appl. Meteorol.* **43**, 170–181 (2004)
- Khain, A.P., Beheng, K.D., Heymsfield, A., Korolev, A., Krichak, S.O., Levin, Z., Pinsky, M., Phillips, V., Prabhakaran, T., Teller, A., van den Heever, S.C., Yano, J.-I.: Representation of microphysical processes in cloud-resolving models: spectral (bin) microphysics versus bulk parameterization. *Rev. Geophys.* **53**, 247–322 (2015)
- Kim, H.-J., Jung, W., Suh, S.-H., Lee, D.-I., You, C.-H.: The characteristics of raindrop size distribution at windward and leeward side over mountain area. *Remote Sens.* **14**, 2419 (2022)
- Lee, H., Baik, J.-J.: A comparative study of bin and bulk cloud microphysics schemes in simulating a heavy precipitation case. *Atmosphere* **9**, 475 (2018)
- Lee, M.-T., Lin, P.-L., Chang, W.-Y., Seela, B.K., Janapati, J.: Microphysical characteristics and types of precipitation for different seasons over north Taiwan. *J. Meteorol. Soc. Jpn.* **97**, 841–865 (2019)
- Lei, H., Guo, J., Chen, D., Yang, J.: Systematic bias in the prediction of warm-rain hydrometeors in the WDM6 microphysics scheme and modifications. *J. Geophys. Res. Atmos.* **125**, e2019JD030756 (2020)
- Lim, K.-S.S., Hong, S.-Y.: Development of an effective double-moment cloud microphysics scheme with prognostic cloud condensation nuclei (CCN) for weather and climate models. *Mon. Weather Rev.* **138**, 1587–1612 (2010)
- Loh, J.L., Lee, D.-I., You, C.H.: Inter-comparison of DSDs between Jincheon and Miryang at South Korea. *Atmos. Res.* **227**, 52–65 (2019)
- Marshall, J.S., Palmer, W.M.: The distribution of raindrops with size. *J. Meteorol.* **5**, 165–166 (1948)
- Milbrandt, J.A., Yau, M.K.: A multimoment bulk microphysics parameterization. Part II: a proposed three-moment closure and scheme description. *J. Atmos. Sci.* **62**, 3065–3081 (2005)
- Mlawer, E.J., Taubman, S.J., Brown, P.D., Iacono, M.J., Clough, S.A.: Radiative transfer for inhomogeneous atmospheres: RRTM, a validated correlated-k model for the longwave. *J. Geophys. Res.* **102**, 16663–16682 (1997)
- Morrison, H., Curry, J.A., Khorostyanov, V.I.: A new double-moment microphysics parameterization for application in cloud and climate models. Part I: description. *J. Atmos. Sci.* **62**, 1665–1677 (2005)
- Pan, Y., Xue, M., Ge, G.: Incorporating diagnosed intercept parameters and the graupel category within the ARPS cloud analysis system for the initialization of double-moment microphysics: testing with a squall line over South China. *Mon. Weather Rev.* **144**, 371–392 (2016)
- Seela, B.K., Janapati, J., Lin, P.-L., Wang, P.K., Lee, M.-T.: Raindrop size distribution characteristics of summer and winter season rainfall over north Taiwan. *J. Geophys. Res. Atmos.* **123**, 11602–11624 (2018)
- Skamarock, W.C., Klemp, J.B., Dudhia, J., Gill, D.O., Liu, Z., Berner, J., et al.: A Description of the Advanced Research WRF Model Version 4 (NCAR technical notes NCAR/TN-556+STR, 145 pp.). National Center for Atmospheric Research, Boulder, CO (2019)
- Suh, S.-H., Kim, H.-J., Lee, D.-I., Kim, T.-H.: Geographical characteristics of raindrop size distribution in the southern parts of South Korea. *J. Appl. Meteorol. Climatol.* **60**, 157–169 (2021)

- Suh, S.-H., You, C.-H., Lee, D.-I.: Climatological characteristics of raindrop size distributions in Busan, Republic of Korea. *Hydrol. Earth Syst. Sci.* **20**, 193–207 (2016)
- Tewari, M., Chen, F., Wang, W., Dudhia, J., LeMone, M.A., Mitchell, K., et al.: Implementation and verification of the unified Noah land surface model in the WRF model. Paper presented at 20th Conference on Weather Analysis and Forecasting/16th Conference on Numerical Weather Prediction, American Meteorological Society, Seattle, WA, USA (2004)
- Thompson, G., Field, P.R., Rasmussen, R.M., Hall, W.D.: Explicit forecasts of winter precipitation using an improved bulk microphysics scheme. Part II: implementation of a new snow parameterization. *Mon. Weather Rev.* **136**, 5095–5115 (2008)
- Thurai, M., Gatlin, P.N., Bringi, V.N.: Separating stratiform and convective rain types based on the drop size distribution characteristics using 2D video disdrometer data. *Atmos. Res.* **169**, 416–423 (2016)
- Tokay, A., Short, D.A.: Evidence from tropical raindrop spectra of the origin of rain from stratiform versus convective clouds. *J. Appl. Meteorol.* **35**, 355–371 (1996)
- Tokay, A., Wolff, D.B., Petersen, W.A.: Evaluation of the new version of the laser-optical disdrometer, OTT Parsivel2. *J. Atmos. Ocean. Technol.* **31**, 1276–1288 (2014)
- Uijlenhoet, R., Steiner, M., Smith, J.A.: Variability of raindrop size distributions in a squall line and implications for radar rainfall estimation. *J. Hydrometeorol.* **4**, 43–61 (2003)
- Wainwright, C.E., Dawson, D.T., Xue, M., Zhang, G.: Diagnosing the intercept parameters of the exponential drop size distributions in a single-moment microphysics scheme and impact on supercell storm simulations. *J. Appl. Meteorol. Climatol.* **53**, 2072–2090 (2014)
- Waldvogel, A.: The N_0 jump of raindrop spectra. *J. Atmos. Sci.* **31**, 1067–1078 (1974)
- Walters, D., Baran, A.J., Boutle, I., Brooks, M., Earnshaw, P., Edwards, J., et al.: The Met Office Unified Model Global Atmosphere 7.0/7.1 and JULES Global Land 7.0 configurations. *Geosci. Model Dev.* **12**, 1909–1963 (2019)
- Yang, Q., Dai, Q., Han, D., Chen, Y., Zhang, S.: Sensitivity analysis of raindrop size distribution parameterizations in WRF rainfall simulation. *Atmos. Res.* **228**, 1–13 (2019)
- You, C.-H., Lee, D.-I., Kang, M.-Y., Kim, H.-J.: Classification of rain types using drop size distributions and polarimetric radar: case study of a 2014 flooding event in Korea. *Atmos. Res.* **181**, 211–219 (2016)
- Zhang, G., Xue, M., Cao, Q., Dawson, D.: Diagnosing the intercept parameter for exponential raindrop size distribution based on video disdrometer observations: model development. *J. Appl. Meteorol. Climatol.* **47**, 2983–2992 (2008)

Publisher's Note Springer Nature remains neutral with regard to jurisdictional claims in published maps and institutional affiliations.